Thermal Decomposition of Energetic Materials. 5. Reaction Processes of 1,3,5-Trinitrohexahydro-*s*-triazine below Its Melting Point

Sean Maharrey and Richard Behrens, Jr.*

Combustion Research Facility, Sandia National Laboratories, Livermore, California 94551-0969

Received: July 28, 2005; In Final Form: October 6, 2005

Through the use of simultaneous thermogravimetry modulated beam mass spectrometry, optical microscopy, hot-stage time-lapsed microscopy, and scanning electron microscopy measurements, the physical and chemical processes that control the thermal decomposition of 1,3,5-trinitrohexahydro-*s*-triazine (RDX) below its melting point (160−189 °C) have been identified. Two gas-phase reactions of RDX are predominant during the early stages of an experiment. One involves the loss of HONO and HNO and leads to the formation of H_2O, NO, NO_2, and oxy-*s*-triazine (OST) or *s*-triazine. The other involves the reaction of NO with RDX to form NO_2 and 1-nitroso-3,5-dinitrohexahydro-s-triazine (ONDNTA), which subsequently decomposes to form a set of products of which CH_2O and N_2O are the most abundant. Products from the gas-phase RDX decomposition reactions, such as ONDNTA, deposit on the surface of the RDX particles and lead to the development of a new set of reaction pathways that occur on the surface of the RDX particles. The initial surface reactions occur on surfaces of those RDX particles in the sample that can accumulate the greatest amount of products from the gas-phase reactions. Initial surface reactions are characterized by the formation of islands of reactivity on the RDX surface and lead to the development of an orange-colored nonvolatile residue (NVR) film on the surface of the RDX particles. The NVR film is most likely formed via the decomposition of ONDNTA on the surface of the RDX particles. The NVR film is a nonstoichiometric and dynamic material, which reacts directly with RDX and ONDNTA, and is composed of remnants from RDX and ONDNTA molecules that have reacted with the NVR. Reactions involving the NVR become dominant during the later stage of the decomposition process. The NVR reacts with RDX to form ONDNTA via abstraction of an oxygen atom from an NO_2 group. ONDNTA may undergo rapid loss of N_2 and NO_2 with the remaining portion of the molecule being incorporated into the dynamic NVR. The dynamic NVR also decomposes and leads to the formation of H_2O, CH_2O, N_2O, NH_2CHO, $(CH_3)_2NCHO$, $(CH_3)_2NNO$, $C_2H_2N_2O$, and $(CH_3)_3N$ or CH_3NCH_2-CH_3. The competition between reaction of the dynamic NVR with RDX and its own thermal decomposition manifests itself in a rapid increase in the rate of evolution of the NVR decomposition products as the amount of RDX remaining in the sample nears depletion. The reactions between the NVR film and RDX on the surface of the RDX particles leads to a localized environment that creates a layer of molten RDX on the surface of the particles where reactions associated with the liquid-phase decomposition of RDX may occur. The combination of these reaction processes leads to an acceleration of the reaction rate in the later stage of the decomposition process and creates an apparent reaction rate behavior that has been referred to as autocatalytic in many previous studies of RDX decomposition. A reaction scheme summarizing the reaction pathways that contribute to the decomposition of RDX below its melting point is presented.

Introduction

A major challenge for today's chemical kineticist is to understand and characterize the complex nonlinear spatiotemporal reaction processes that control the decomposition of explosive organic compounds, such as 1,3,5-trinitohexahydro-*s*-triazine (RDX, Scheme 1) in reaction environments that are relevant for assessing their aging, safety, and combustion characteristics. While many studies of this compound over the past 50 years have focused on characterizing its thermal decomposition and reactions in combustive environments, an understanding of the underlying reaction process has been difficult to develop.[1−6] Most experimental studies have focused on examining its thermal decomposition at temperatures (20−300 °C) well below those associated with combustion due to experimental feasibility and expediency. The initial reaction schemes used to characterize the reaction processes that control its decomposition have been based on gas-phase reaction rate concepts in which unimolecular decomposition theory may be used to estimate reaction rates based on the calculation of

SCHEME 1. Decomposition Pathways of RDX above Its Melting Point

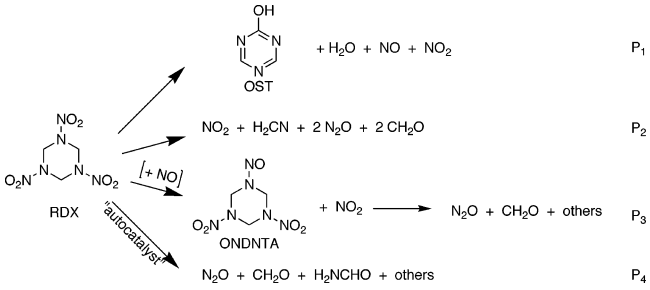

* To whom correspondence may be addressed. E-mail: rbehren@sandia.gov. Phone: (925) 294-2170. Fax: (925) 294-2170.

10.1021/jp054188q CCC: $30.25
Published on Web 11/18/2005

activation energies for various decomposition pathways using various forms and levels of theory.[7,8] Examination of the literature reveals few experimental studies on the decomposition of RDX that are limited to examining exclusively gas-phase, single-molecule aspects of its decomposition. An infrared multiphoton dissociation (IRMPD) study of RDX[9] provides the only experimental results on its gas-phase, single-molecule decomposition pathways. The results obtained in most other studies involve contributions from reactions that occur in the condensed phase.

Simultaneous thermogravimetric modulated beam mass spectrometry (STMBMS) experiments with RDX above its melting point[10,11] revealed how additional complexity, beyond single-molecule reaction processes, is introduced into the reaction processes that control the thermal decomposition of RDX. The results showed that four different primary reaction pathways control the decomposition of RDX in the liquid phase (Scheme 1). The first pathway (P1) is the direct decomposition of RDX via loss of HONO and HNO from RDX, which results in the formation of oxy-*s*-triazine (OST). Subsequent reactions of HONO produce the H_2O, NO, and NO_2 products. The mechanistic aspects of this pathway were strongly supported by the experimental results. The second pathway (P2) is consistent with a concerted ring fragmentation leading to the formation of three methylenenitramine (H_2CNNO_2) moieties, which undergo subsequent reactions to form NO_2, H_2CN, N_2O, and CH_2O. The experimental evidence supporting the mechanistic details of the pathway P2 is limited and cannot explicitly verify the formation of the observed products via the concerted ring fragmentation mechanism. The third pathway (P3) involves a substitution reaction in which an RDX NO_2 group is replaced by NO and results in the formation of 1-nitroso-3,5-dinitrohexahydro-*s*-triazine (ONDNTA), the mononitroso analogue of RDX. Subsequent reaction of this intermediate is quite complex and results in the formation of N_2O and CH_2O and a set of other products. This intermediate has been synthesized and its decomposition examined in STMBMS experiments.[12] The results revealed that a complex process controls the decomposition of ONDNTA and that this process is consistent with the behavior observed in the decomposition of RDX. The fourth pathway (P4) involves an "autocatalytic-like" reaction of RDX with a product that accumulates in the sample as an experiment progresses and produces N_2O, CH_2O, NO_2, and NH_2CHO. Subsequent experiments with ONDNTA suggest that pathway P4 may also involve the ONDNTA reaction intermediate, in which the ONDNTA leads to the formation of a nonvolatile residue (NVR) that interacts with RDX and leads to a time-dependent change in the rate of decomposition that could be interpreted as being autocatalytic.

The four reaction pathways include two direct decomposition reactions of RDX, similar to the

$$\mathrm{RDX} \rightarrow 3\mathrm{HCN} + 3\mathrm{HONO} \qquad \text{(R1)}$$

$$\mathrm{RDX} \rightarrow 3\,\mathrm{CH_2O} + 3\,\mathrm{N_2O} \qquad \text{(R2)}$$

reactions used to characterize RDX decomposition at high heating rates[13] and two additional pathways that are more complex. If only reactions such as R1 and R2 controlled the decomposition of RDX, then the associated reaction kinetics would be simple and relatively easy to characterize. However, reaction pathway P3 involves interactions with a gaseous decomposition product, creating a coupling between reaction pathways and introducing nonlinear effects into the underlying reaction kinetics. Furthermore, in reaction pathway P4, a nonvolatile reaction product accumulates in the sample and reacts with the remaining RDX. This behavior introduces an " arrow of time" into the reaction process and imposes a temporal dependence in which the relative contributions from the underlying reaction pathways change during the course of an experiment. Careful comparison of the rates of evolution of the various decomposition products from STMBMS experiments with RDX[10,11] shows that contributions from the underlying reactions change continuously during the course of an experiment. This variation in reaction features also has been observed in thermogravimetric analysis (TGA) and differential scanning calorimetry (DSC) experiments with RDX as evidenced by changes in the activation energies during the course of an experiment.[14] Hence, the reaction processes that control the decomposition of RDX are at least complex, nonlinear, and temporally dependent.

In this paper, the processes that control the decomposition of RDX below its melting point and how they are related to the four reaction pathways observed in its liquid-phase decomposition are examined. The thermal decomposition of RDX below its melting point has been examined previously by Cosgrove and Owen,[15,16] Batten,[17−21]and Bradley et al.[22] Their results provide qualitative insight into the features of the solid-phase decomposition process, show the effects of varying the pressure and types of gases confined with the sample, and demonstrate that higher gas confinement promotes an "auto-catalytic-like" decomposition process. In this paper, we address the following outstanding issues regarding the decomposition of RDX: (1) How the reaction pathways observed in the liquid-phase decomposition of RDX are related to the physicochemical processes that control its decomposition below the melting point. (2) The role of gas-phase reactions in the decomposition process. In experiments with RDX above its melting point, reactions in the liquid dominate and contributions from gas-phase RDX decomposition processes are difficult to distinguish. Below its melting point, contributions from the decomposition of gaseous RDX are more readily observed. (3) Reactions that control the decomposition of RDX in the particles. Whether or not reactions occur directly in the solid phase or if reactions in the gas phase are required to create new reaction pathways in the solid are examined.

To address these issues, results from experiments that focus on identifying the main chemical reactions and physical processes that control its decomposition between 170 and 189 °C are presented. The results show that the underlying reaction processes that control the decomposition are complex and involve reactions that occur in both the gas phase and on the surface of the RDX particles.

Experimental Methods

Instrument Description. An overview[23] describes the experimental methods and numerical algorithms used to examine and characterize the reactions of energetic materials in the condensed phase at low and moderate temperatures and details of the STMBMS instrument and analysis methods have been described previously.[24−26] The experimental methods utilize: (1) the STMBMS instrument to conduct thermal decomposition experiments and an associated set of numerical algorithms to transform the raw data to rates of formation of the decomposition products, (2) isotopically labeled analogues or a Fourier transform ion cyclotron resonance (FTICR) mass spectrometer to aid in identifying the products, and (3) scanning electron microscopy (SEM) to examine the morphological aspects of the reaction processes. Qualitative models of the spatiotemporal-

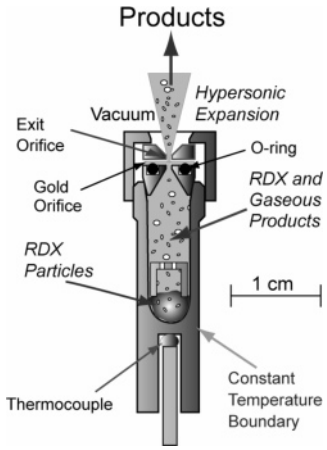

Figure 1. Cross section of reaction cell. Reaction cell is constructed from aluminum oxide, 99.8% purity. Reaction cell is sealed with ground fit cone and elastomer O ring beneath gold foil orifice. Baffle above sample reduces splatter onto gold orifice.

dependent reaction processes that control the decomposition of RDX are developed from data collected with these three methods. The methods also provide quantitative data that may be used to develop mathematical models of the underlying reaction processes.[27,28]

The basic features of a thermal decomposition experiment using the STMBMS instrument are illustrated in Figure 1. A small sample of RDX (2−10 mg) is placed in an alumina reaction cell (free volume of 0.227 cm^3), which is sealed with a cap assembly containing a disk of gold foil (25μm thick) that contains a hole with a specific diameter (2.5−50 μm) through its center. The reaction cell is heated in a controlled manner, using the thermocouple to measure and control the temperature of the cell. As the reaction cell is heated, vapor from RDX, and any other compounds within the cell, fills the free volume. The vapor flows through the orifice, and each constituent is identified and its rate of flow through the orifice is determined. The measurements provide the time-dependent *rate of formation* of each gaseous species that is present *solely* in the gas phase within the reaction cell. The measurements also provide the *vapor pressure* of gaseous species that are in *quasi-equilibrium* with material in condensed phases. For example, during the decomposition of RDX above its melting point, ONDNTA forms a solution with RDX, and the amount of ONDNTA vapor present in the gas phase is proportional to its mole fraction in the liquid. Thus, data on the rate of formation of both gas and condensed phase species are obtained during the course of an experiment.

The pressure of gases confined within the reaction cell, at a given temperature, may be varied by using orifices with different diameters and/or varying the mass of the sample. The gas pressure within the cell is governed by a steady-state balance between the rate of gas formation from the sample and the rate of exhaust through the orifice. Smaller orifices will result in higher pressures for a given gas formation rate from the sample. For compounds in a two-phase quasi-equilibrium, the pressure is governed by the temperature of the reaction cell and the properties of the compounds. In this case, a smaller orifice results in a lower rate of the gas exiting the reaction cell.

The data used to characterize the thermal decomposition processes are the identities and rates of formation of the different vapors that flow through the orifice and out of the reaction cell over a range of experimental conditions. The reaction conditions are controlled by altering the sample size, temperature, heating rate, orifice diameter, and volume of the reaction cell. For experiments with powders, the average particle diameter may be altered to assess effects of surface area on the rates of reaction.

Two modifications have been made to the original experimental and data analysis procedures.[24−26] First, to contain higher pressures of gas within the reaction cell during an experiment, the cap assembly of the reaction cell assembly now includes a gold orifice fitted with an elastomer O-ring seal and a thin bead of Krytox ultrahigh vacuum grease is applied to the ground cone to obtain a reproducible seal. After loading the sample, the reaction cell assembly is checked with a Balzers model HLT 160 helium leak detector to verify that the cell is properly sealed and gases will only evolve through the orifice. Second, a new procedure has been developed to calibrate the flow rate through the gold orifices and provide an accurate representation of the pressure within the reaction cell. In this procedure a standard set of orifices was created to relate the pressure within the reaction cell to the flow rate of gas through the ionization region of the mass spectrometer, which is used to detect the gases. The standard set of orifices was calibrated using naphthalene as the source of vapor in the reaction cell. This calibration provides a measure of the fraction of gas that exits the cell and flows through the ionization volume of the mass spectrometer as a function of pressure within the cell. To relate the flow characteristics of a gold orifice used in individual experiments to the flow characteristics of an orifice in the standard set of calibration orifices, a flow test system is used to measure the flow rate of nitrogen through the orifices. Pressure correction factors for each experiment are obtained by comparing the nitrogen flow rates through the orifice used in an experiment with the nitrogen flow rates measured for the corresponding calibration orifice. The measurements are made before and after each experiment to check whether the flow rate through the orifice has been altered during the course of an experiment. The equivalent "choked" flow orifice diameter and gas holding time within the fixed reaction cell volume are also calculated from the nitrogen flow tests, which allows orifices to be matched as closely as possible for given experiments and allows for better control of orifice diameter as an experimental variable.

The mass range of the quadrupole mass spectrometer is calibrated using perfluorotributylamine. The resolution is set so that the peak widths in the 20−300-amu region are approximately 0.7 amu full width at 10% maximum. The ionizer is operated in the linear electron-emission range at 1.0 mA. The electron energy is calibrated using the appearance potential of H_2O and set to 20 eV for all experiments, to reduce ion fragmentation in the mass spectrometer.

Hot-Stage Time-Lapse Microscopy. The hot-stage microscopy system used to examine the morphological changes in RDX particles as they decompose is shown in Figure 2. The system consists of a nitrogen gas convective hot-stage (Fluid Inc.), an Olympus SZH stereo optical microscope, a Polaroid model DMC digital microscope camera with DMC Direct 1.0 image acquisition software, and a G4 Macintosh computer for image acquisition. Individual particles of RDX were placed in a quartz sample cell (0.026 cm^3 free volume). The quartz cell was mounted in a thermally insulated cooling block and a methane/oxygen mini-torch was used to neck-down the end of the cell to a small throat diameter (<50 μm). The complete microreactor was then mounted under the thermocouple probe tip within the optically accessible hot-stage. The microreactor was heated and held at an isothermal temperature

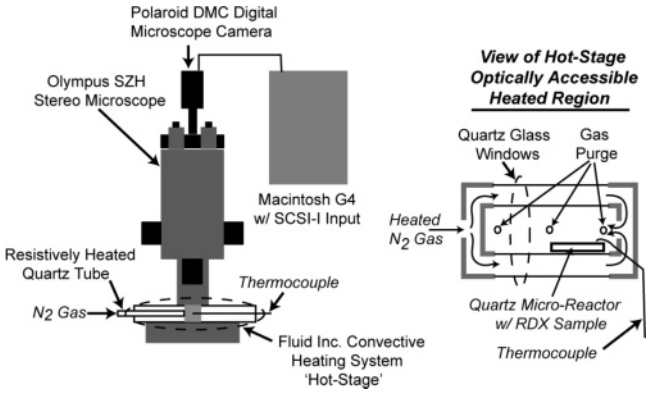

Figure 2. Schematic illustration of hot-stage microscope apparatus used for time-lapse microscopy measurements. The RDX sample is placed in the quartz microreactor, which is then placed in the optically accessible convective heating system and heated with N_2 at a pressure of 0.237 MPa.

below the melting point of RDX, and time-lapse photographs of the RDX particle were recorded at set intervals during the experiment.

Sample Preparation. Warning RDX is a High Explosive and Must Be Handled in an Appropriate Manner. The pure RDX samples used in these experiments were prepared by oxidation of hexahydro-1,3,5-trinitroso-*s*-triazine.[11] The mean RDX particle size used in these experiments was 194 μm, as measured with particle-sieving methods. The RDX particles for hot-stage microscopy were grown by dissolving pure (>99%) RDX powders in high-purity acetone and slowly recrystallizing the RDX over 7−10 days. This recrystallization process produced single large particles of RDX ranging from 1 to 6 mg.

Results

To probe the decomposition of RDX below its melting point, a set of experiments was conducted over a range of experimental conditions. Results from these experiments provide insight into reaction processes associated with sublimation and decomposition of RDX in the gas-phase, condensed-phase decomposition, and the reaction processes that lead to the development of complex nonlinear spatiotemporal processes on the surface of the RDX particles. First, the identities of the products formed during the decomposition are presented. Next, the temporal dependence of the rates of decomposition over a range of different experimental conditions is described. The variation in the rates of decomposition is illustrated with both simple TGA results and the rates of evolution of the various gas products during the course of each experiment. The TGA results illustrate the overall trends in the reaction processes over a range of different conditions, and the rates of gas evolution of individual products provide insight into contributions from the underlying reaction pathways. After describing the various processes revealed by the TGA data, optical and SEM pictures of RDX taken during different stages of the decomposition processes are presented to illustrate the morphological features associated with the reaction processes. Next, the products associated with the various underlying thermal decomposition processes are described. Finally, data illustrating the interaction of RDX with the NVR is presented. Table 1 lists five representative experiments conducted over a range of experimental conditions.

Product Identities. The identities of the products formed during the decomposition of RDX in these experiments are listed in Table 2. Products are listed by the *m*/*z* values used to measure each product with the mass spectrometer. The identities of the products associated with each *m*/*z* value have been determined from molecular weights derived from previous time-of-flight velocity spectra (TOFVS) experiments[29] and their corresponding molecular formulas, as derived from previous STMBMS experiments with isotopically labeled analogues of RDX.[11] In addition to the gaseous products listed in Table 2, a dark-red to orange colored remnant from the dynamic NVR remains in the reaction cell at the conclusion of the experiments. The amount of NVR remaining at the end of each experiment is listed in Table 1. Elemental analysis of two NVR samples shows that it is enriched in carbon and hydrogen compared to RDX and has a molecular formula of C, 3; H, 5; N, 1.7−1.8; O, 2−2.3.

TGA Data. Trends in the temporal dependence of the total sample mass vs time curves provide a global overview and initial insight into the general behavior and the degree of complexity of the decomposition process under a particular set of experimental conditions. The temporal behavior of the TGA data is correlated with the evolution of specific products, which provides insight into the chemical reactions associated with the underlying reaction processes. To depict the primary underlying reaction processes that contribute to the overall decomposition behavior of RDX below its melting point, data is presented from a series of experiments in which temperature and pressure of the gaseous products confined with the sample are varied (parts A and B of Figure 3). The role of the NVR is depicted by

TABLE 1: Experimental Parameters

exp. no.	temperature (°C)	orifice diameter (μm)	Choked-flow diameter (μm)	sample mass (mg)	decomp.[a] time (s)	residue mass (mg)
I	179	10	10.65	8.12	85 896	0.65[c]
II	179	5	7.28	8.33	73 595	0.79[d]
III	184	5	5.20	9.41	50 695	0.93[d]
IV	189	5	na	8.01	41 665	0.61[d]
V	179	5	6.29	14.3[b]	42 042	1.86[c]

[a] Time measured from start of isothermal condition. [b] Added onto 0.33 mg of residue from a 5 μm, 180 °C experiment. [c] Residue mass measured by Mettler balance in STMBMS apparatus. [d] Residue recovered from reaction cell and weighed.

TABLE 2: Decomposition Products from RDX

ion *m*/*z* value[a]	STMBMS-derived molecular formula ($C_xH_yN_zO_w$)[b]
18	H_2O
27	HCN
28	CO, N_2, RDX[c]
29	CH_2O, RDX[c]
30	CH_2O, NO, RDX[c]
43	C_2H_5N
44	N_2O
45	H_2NCHO
46	NO_2, RDX[c]
47	HONO
58	C_3H_9N[d]
59	CH_3NHCHO[e]
70	$C_2H_2N_2O$[f]
73	$(CH_3)_2NCHO$
74	$(CH_3)_2NNO$
81	$C_3H_3N_3$
97	$C_3H_3N_3O$ (OST)
132	$C_3H_6N_6O_5$ (ONDNTA)
128	$C_3H_6N_6O_6$ (RDX[c])

[a] *m*/*z* values of ions formed in mass spectrometer from the products formed in the reaction cell during an experiment. [b] Neutral products represented by the measured *m*/*z* values. [c] Electron bombardment fragment of RDX. [d] May be either $(CH_3)_3N$ or $CH_3NCH_2CH_3$. [e] Time-of-flight analysis indicates this product formed as a dimer.[10] [f] Originates from a product formed in NVR reactions and from ion fragment of OST.

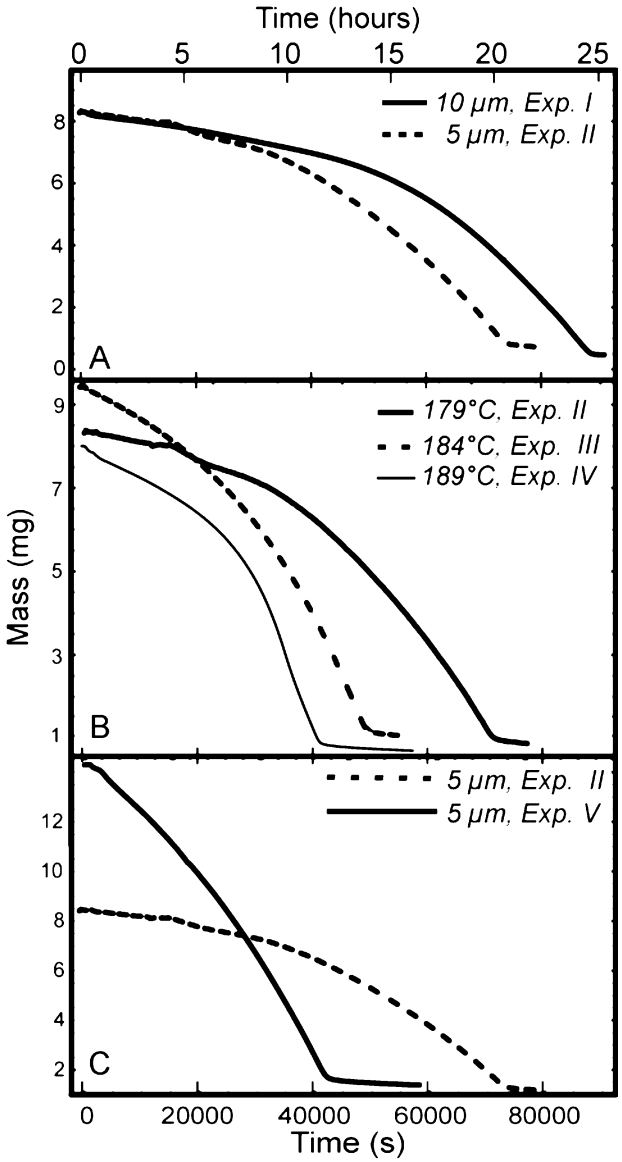

Figure 3. Mass of sample vs time for Exps I−V. Panel A shows results illustrating the effect of pressure of the gaseous decomposition products on the rate of mass loss. Panel B shows results illustrating the effect of temperature on the rate of mass loss. Panel C shows results illustrating the effect of the NVR on the rate of mass loss.

comparing the decomposition behavior from an experiment with a mixture of NVR and RDX (Exp. V, Figure 3C) with a similar experiment using only RDX (Exp. II).

The effect of gas confinement on the decomposition process is illustrated in Figure 3A with data from two experiments in which the orifice diameter is decreased from 10 to 5μm (Exps. I and II). While RDX does decompose in the gas phase, as indicated in the results from STMBMS measurements described below (Figure 7), the isothermal TGA results are unable to distinguish mass loss due to RDX vapor exiting the reaction cell from mass loss due to the RDX gas-phase decomposition products exiting the reaction cell.

At the lower gas confinement, the mass loss rate from Exp. I (10-μm orifice) is approximately constant during the first 20 000 s of the experiment (~0.09 mg/h) and then accelerates through the remainder of the experiment, reaching a final rate of mass loss of 0.70 mg/h when the RDX is near depletion at ~86 000 s. Mass loss due to both decomposition products formed from RDX in the gas phase and RDX vapor exiting the reaction cell is consistent with the constant rate of mass loss observed during the first 20 000 s of the experiment. The accelerating rate of mass loss, starting at ~20 000 s, indicates that additional reaction processes occur, other than RDX sublimation or decomposition of RDX in the gas phase. These additional processes involve reactions associated with the condensed phase of RDX and indicate a change in the rate controlling mechanism during the course of the experiment. The continually increasing rate of mass loss during the course of the experiment indicates that the reaction rates associated with the condensed phase reaction processes do not depend solely on the mass of RDX available for reaction.

At higher gas confinement, the qualitative features of the mass loss from Exp. II with the 5-μm orifice are similar to Exp. I with the 10-μm orifice. In this case, the mass loss rate is again approximately constant during the first 20 000 seconds of the experiment (~0.10 mg/h) and then accelerates through the remainder of the experiment, reaching a final rate of mass loss of 0.72 mg/h when the RDX is near depletion at ~74 000 s. The almost identical mass loss rates during the first 20 000 s of Exps. I and II indicate that most of the mass loss during this stage of the experiment arises from evolution of lower molecular weight products formed in the gas-phase decomposition of RDX, rather than the evolution of RDX itself from the reaction cell. On the basis of the effective choked flow diameters of the orifices used in each experiment (Table 1), the pressure of the gaseous decomposition products within the reaction cell should be about twice as high in Exp. II compared to Exp. I. In contrast to Exp. I, the acceleration in the rate of decomposition is faster in Exp. II, indicating a faster build up of the contributions from reactions associated with condensed phase processes. The similar time to onset of the acceleratory reaction rates in each experiment suggests that the reactions that lead to the nucleation conditions required for condensed phase processes to commence is similar in both experiments. However, once the nucleation conditions are established, higher pressure of one, or more, of the decomposition products results in the more rapid development of the reactions that control the condensed phase processes. Furthermore, the nearly identical final mass loss rates of Exps. I and II (0.70 vs 0.72 mg/h) indicate that, once the condensed-phase processes are developed, the rate-limiting steps may no longer be dependent on the products formed via the decomposition of RDX in the gas phase.

Further insight into reaction processes that occur below the melting point of RDX has been obtained by examining its decomposition between 179 and 189 °C (Exps. II, III, and IV). The TGA results are shown in Figure 3B, and the corresponding gas evolution rates (GERs) of the decomposition products from the reaction cell are described below and shown in Figure 8. The TGA results at 179 °C (Exp. II) and 184 °C (Exp. III) exhibit an initial constant rate of decomposition followed by an accelerating rate of decomposition. In Exp. III, the duration of the initial constant rate of decomposition is shorter and difficult to distinguish from the TGA data. (However, reaction products associated with primarily gas-phase decomposition during the early stage of decomposition are apparent in the corresponding data presented in Figure 8.) In Exp. III (184 °C) the mass loss rate is approximately constant during the first 5 000 s of the experiment (~0.28 mg/h) and then accelerates through the remainder of the experiment, reaching a final rate of mass loss of 1.10 mg/h when the RDX is near depletion at ~51 000 s. The fractions of residue formed in Exps. II and III are approximately equal (0.094 and 0.099, respectively, Table 1). Thus, the general behavior of the decomposition processes at 179 and 184 °C is similar.

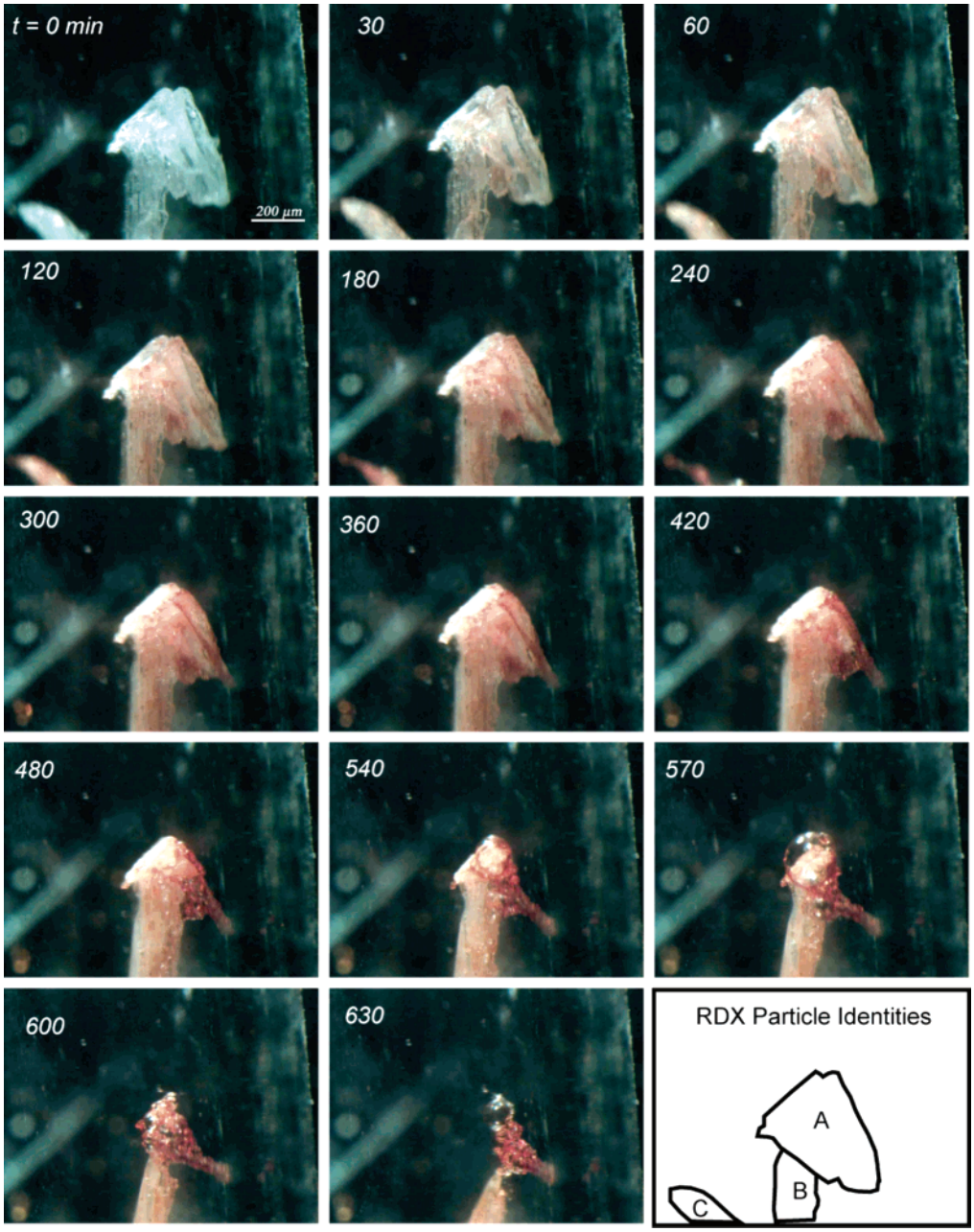

Figure 4. Hot-stage time-lapse images of a 1.6-mg RDX single particle decomposing at 180 °C in a quartz microreactor with a 10-μm diameter exhaust orifice. Time in minutes is listed on each image. $T = 0$ is when the sample first reaches 180 °C.

The temporal behavior of the TGA data from Exp. IV (189 °C) is more complex than the data from the experiments at 179 and 184 °C. In Exp. IV, the decomposition behavior over the first 20 000 s of the experiment is similar to the behavior observed in Exp. III (185 °C). The initial rate of mass loss is 0.24 mg/h, compared to 0.28 mg/h in Exp. III. However, in Exp. IV there is a rapid acceleration in the rate of reaction starting at about 20 000 s. This behavior suggests that at 189 °C another type of condensed phase process may develop and contribute to the overall decomposition rate. It is interesting to note that the fraction of residue formed at 189 °C is 0.076, significantly lower than the fraction formed in the two experiments at lower temperatures.

To probe the interaction between RDX and the NVR, experiments were conducted in which RDX was combined with NVR, formed in a previous experiment, and the decomposition of this mixture was examined (Exp. V). The sample for Exp. V was prepared by placing RDX on top of a solid mass of NVR that was formed in a previous experiment at 180 °C using a reaction cell fitted with a 5-μm orifice. The TGA results from Exp. V are shown in Figure 3C, and the corresponding gas evolution rates are shown in Figure 7C. In this case the initial mass loss rate starts at a relatively high value ($\sim$0.77 mg/h) and accelerates slightly through the remainder of the experiment, reaching a final rate of mass loss of 1.55 mg/h when the RDX is near depletion at $\sim$42 000 s. Comparing the results from Exps. V and II (Figure 3C) shows that the initial decomposition rate is higher and the total decomposition time is significantly shorter than in the corresponding experiments with starting samples containing only RDX. This experiment demonstrates that reaction between RDX and the NVR is a dominant reaction pathway below the melting point of RDX. By consideration of the geometric relationship between the RDX and the NVR in Exp. V and the fact that RDX remains a solid during the experiment, the higher initial reaction rate is most likely due to the transport of RDX through the gas phase to the surface of

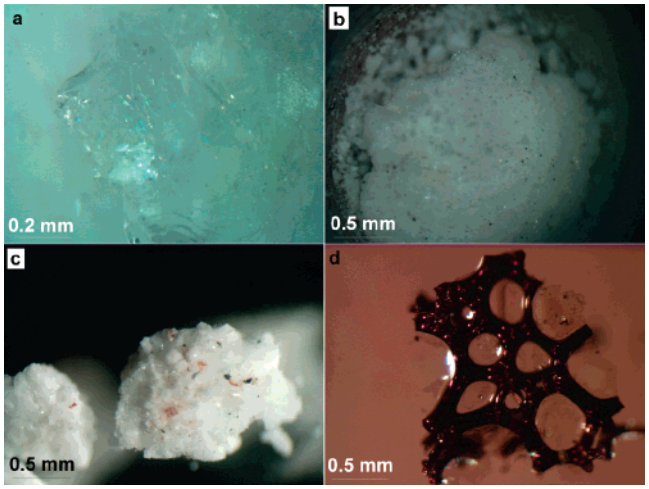

Figure 5. Optical images of RDX samples taken at different stages during the decomposition process. The pictures show the pristine RDX (a), a sample after 3% mass loss (b), as sample after 30% mass loss (c), and the dark-red translucent NVR sample remaining after complete decomposition (d). Background colors differ due to different lighting conditions.

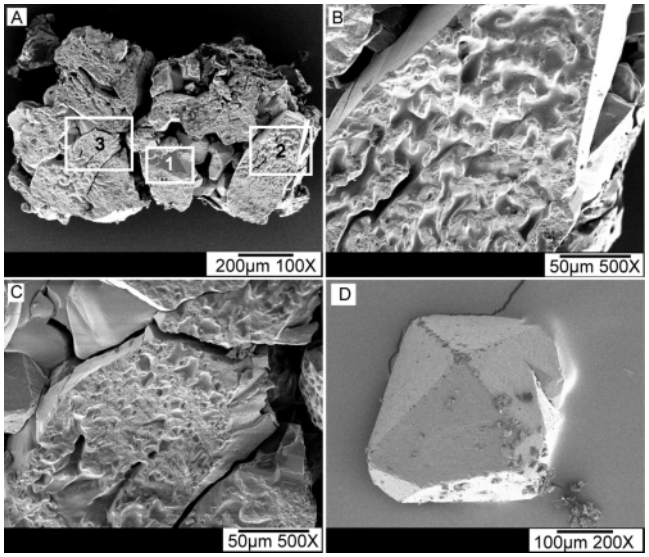

Figure 6. SEM pictures of a partially decomposed agglomerate of RDX particles (A, B, and C) and an inner surface of a fractured pristine RDX particle (D). The agglomerate of RDX was decomposed at 160 °C in a reaction cell with a 5-μm orifice. The sample was quenched after ~35% mass loss. Picture A shows the outer surface of the agglomerate of RDX particles. Higher magnification pictures of regions 2 and 3 are shown in pictures B and C, respectively. In region 1 the agglomerate has fractured during handling and reveals a view into the subsurface of the sintered material, showing an RDX particle with a smooth surface.

the NVR, where it reacts to form the decomposition products. However, it is also possible that as the mixture is heated the NVR in the bottom of the reaction cell becomes molten and interacts with the RDX on the surface of the RDX particles.

Although the relative increase in the rate of reaction in Exp. V is smaller compared to the experiments with samples containing only RDX, the absolute change in the rate of mass loss (1.55 − 0.77 = 0.78 mg/h) is similar to the final rate of mass loss observed in the corresponding experiment (Exp. II). Thus, the accelerating rate of decomposition in Exp. V is most likely due to the nucleation and growth of NVR on the surface of the RDX particles as was the case for Exps. I−IV. In Exp. V, the growth of the reaction rate due to reactions on the surface of RDX particles is masked by the relatively high rate of reaction between RDX and the NVR included from the previous experiment.

Hot-Stage Time-Lapse Microscopy. The TGA and GER results show that the NVR plays a significant role in the controlling the decomposition of RDX. Hot-stage microscopy is used to investigate how and where the NVR is formed during the decomposition of RDX. Results from the hot-stage microscopy experiments provide information on the spatiotemporal features of the underlying reaction processes. A set of time-lapse photographs of a 1.6-mg particle decomposing at 180 °C in a quartz reaction cell is shown in Figure 4. The duration of the experiment was approximately 10 h. The elapsed time in minutes is listed on each picture and a legend identifying particles A, B, and C in each picture is shown.

The first image (t = 0 min) shows the pristine RDX particles at 180 °C. At t = 30 min, the red-colored NVR has started to form on the right side of the particles. The RDX underlying the NVR remains translucent. The red NVR continues to grow (t = 60 and 120 min) until it covers the entire surface of particles A and B and has consumed most of particle C (180 min). Correspondingly, there is little NVR covering the upper left side of the particle A and the left side of particle B. Particle C disappears at 240 min. From 180−360 min, the NVR film is seen to substantially darken and thicken on particles A and B, while not spreading significantly. From 30−360 min a substantial portion of the RDX on the right side of particle A has been consumed in the reaction. At 360 min, a small spot of NVR has formed on the lower right underside of particle A. The region of particle A that is more heavily coated with NVR (right side) reacts more rapidly, as this portion of the RDX particle disappears more rapidly, moving from right to left in the images from t = 360−540 min. When it reaches the unaltered RDX, a bubble rapidly forms and grows while the NVR consumes the unaltered RDX (t = 540−630 min). At 630 min, the NVR bubble ruptures upon depletion of the RDX that formed particle A, leaving an NVR that is morphologically similar to that remaining from the STMBMS experiments. While particle B has formed a thick film coating, it has not fully decomposed during this same time period. The total decomposition time for this experiment was ~37 000 s. The more rapid decomposition of the RDX sample in the hot-stage experiment, compared to a nominally similar STMBMS experiment (Exp. II, 86 000 s), is most likely due to the higher pressure (~0.237 MPa) of the gaseous products contained in the vicinity of the RDX sample in the hot-stage experiments.

Optical Microscopy. The morphology of the NVR that grows on the RDX sample during the STMBMS experiments is less uniform than that observed in the hot-stage decomposition experiments. The growth and development of the NVR during the STMBMS experiments was probed by quenching STMBMS experiments at various extents of decomposition and taking high-magnification optical images of the remaining sample. Figure 5 shows a pristine RDX sample (a), samples that have undergone 3% (b) and 30% (c) mass loss, and the residue remaining after full decomposition (d). The pictures of partially decomposed samples were taken from experiments run at 160 °C using a 5-μm reaction cell exit orifice. During the initial stages of the decomposition (Figure 5B), the individual RDX particles have sintered and formed a white, opaque, rigid matrix. The individual RDX particles are still visible in the surface of the sintered material and upon removal, not shown, from the agglomerate, appear unchanged from the pristine RDX. The next stage of the NVR formation, not shown in Figure 5, involves the

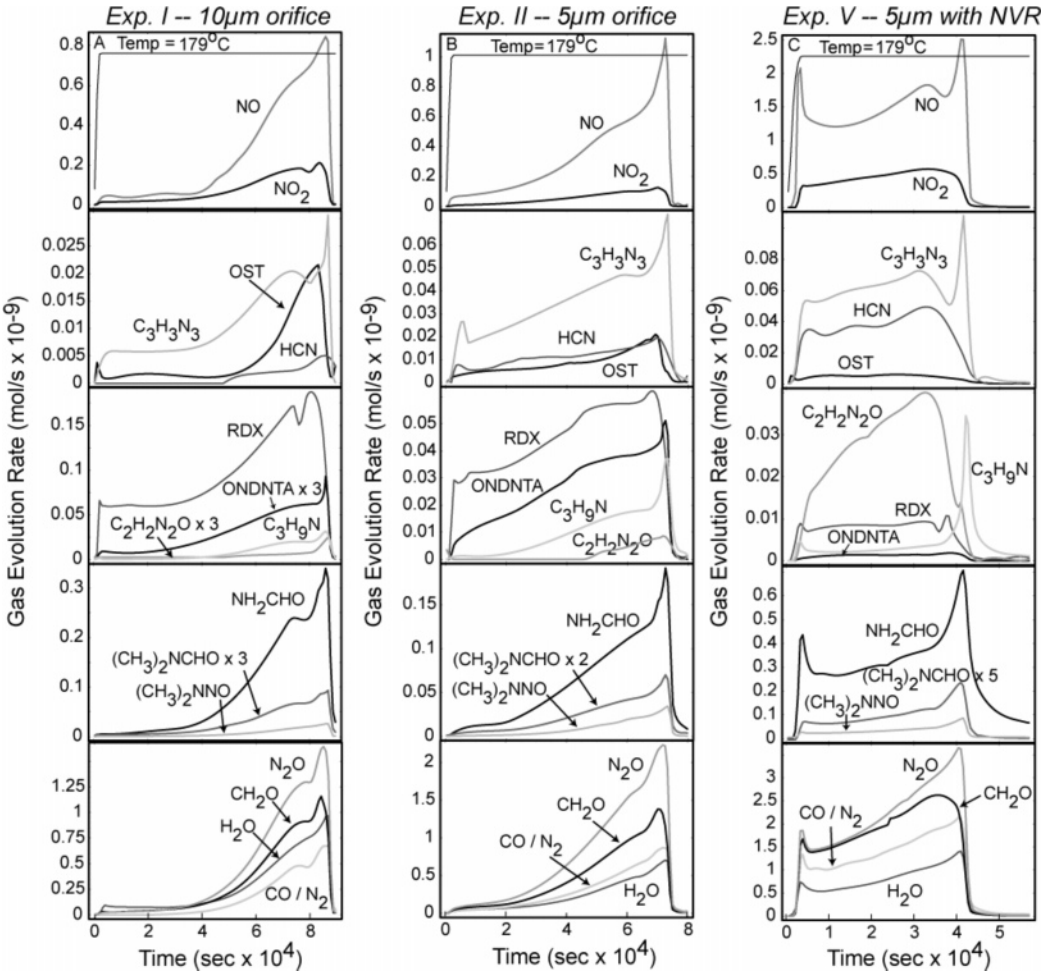

Figure 7. Gas evolution rates of products formed during the decomposition of RDX in three separate experiments conducted under isothermal conditions at 179 °C. Temperature profile is shown in upper panel. The starting temperature for each experiment is 20 °C. (A) Decomposition of RDX using a 10-μm diameter orifice (Exp. I). (B) Decomposition of RDX using a 5-μm diameter orifice (Exp II). (C) Decomposition of mixture of RDX and NVR using a 5-μm diameter orifice (Exp V). Experimental conditions are listed in Table 1.

formation of small, isolated, black "decomposition" spots on the sintered surface. At this stage of the process, the RDX particles are still visible in the sintered surface and appear as pristine RDX. Figure 5c shows the sample at the next stage of the NVR formation process. The RDX particles, which were still visible in the sintered surface of Figure 5b, have been completely covered by the sintered surface and the black spots have grown in size and number. An orange-colored NVR grows in the vicinity of the black spots. The RDX particles lying beneath the sintered surface can be recovered and still appear translucent and unaltered, with no black spots or orange patches growing on them. At the onset of the final stage of the NVR formation, the individual orange-colored regions coalesce into large, reddish-orange-colored translucent fibers that grow together to form the red, translucent NVR, shown in Figure 5D.

While the development of the NVR in the hot-stage and STMBMS experiments is similar, the details of the growth of the morphological characteristics differ and suggest a possible reaction process leading to its formation. The NVR forms a relatively uniform red-colored film on the surface of the particle in the hot-stage experiment (Figure 4, $t = 30$ and 60 min), whereas it forms localized islands situated in RDX that was redeposited in regions between the particles during the ST-MBMS experiments (parts b and c of Figure 5). Although there are differences in the volume and type of materials used to construct the reaction cells used in the hot-stage and STMBMS experiments, the main difference is the pressure of the gaseous decomposition products that are contained in the vicinity of the sample in each type of experiment. The hot-stage experiments are conducted at a constant pressure of 0.237 MPa (1775 Torr). In the STMBMS experiments, the pressure of the products in the reaction cell is determined by the steady-state balance between their rate of formation and their rate of flow out of the reaction cell. For the experiments conducted at 160 °C, using a 5-μm orifice, the pressure during the experiment ranges from 270−9300 Pa (2−70 Torr).

The higher pressure of the gaseous products contained in the quartz microreactor used in the hot-stage experiments will increase the rate of gas-phase reactions and limit the transport of material by diffusion. Thus, in the hot-stage experiments, the gas-phase reactions will be confined more to a layer adjacent to the surface of the particle and less volatile products, formed in gas-phase reactions, are likely to deposit more uniformly on the surface of the particle. In the STMBMS experiments, material transport is greater as evidenced by the deposition of RDX in the sintered regions of the sample, due to relatively rapid sublimation and condensation processes and greater diffusion distances at lower pressure. The products from the gas-phase decomposition reactions apparently deposit and undergo more rapid condensed-phase reactions in the sintered regions of the RDX sample in the STMBMS experiments.

The growth of the dynamic NVR in the hot-stage and STMBMS experiments is consistent with the following general reaction scheme: (1) RDX decomposes in the gas phase, (2)

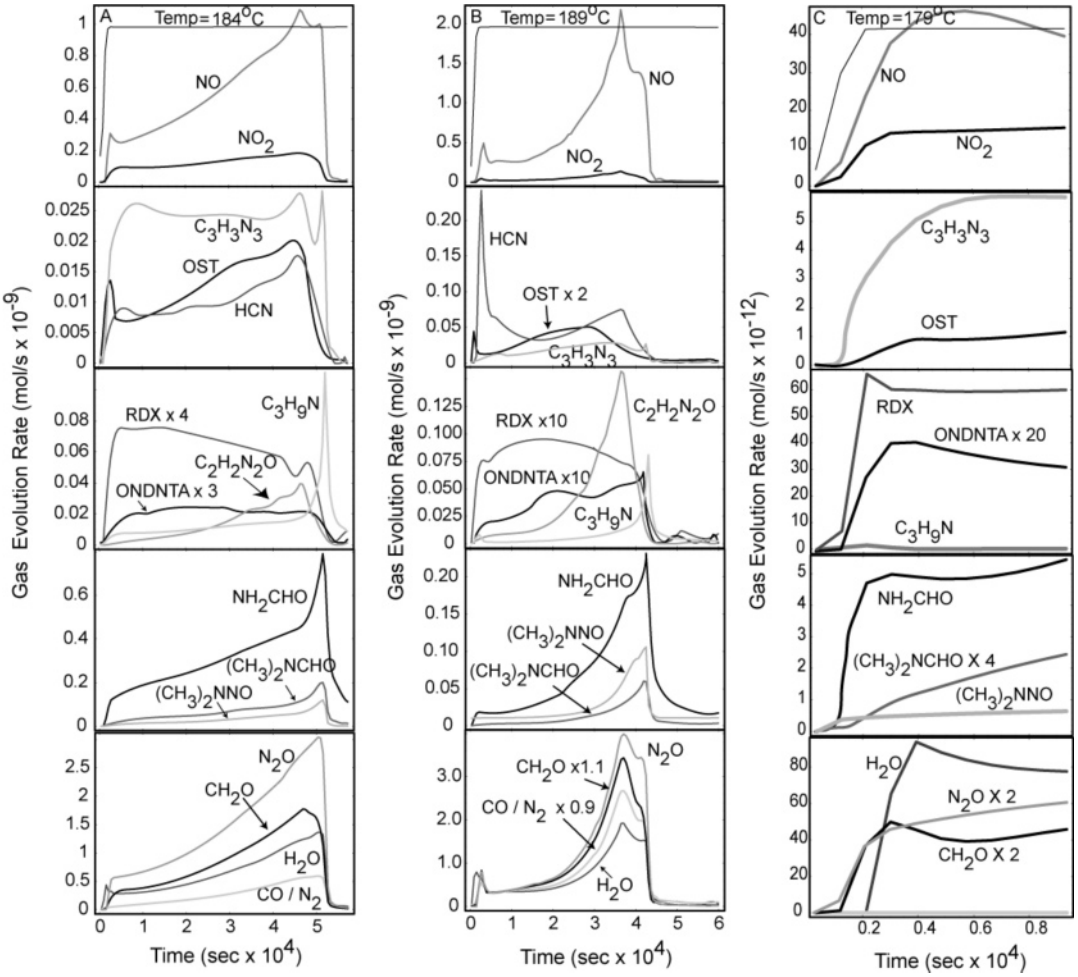

Figure 8. Gas-evolution rates of products formed during the decomposition of RDX at isothermal temperatures of 184 °C (A, Exp. III) and 189 °C (B, Exp IV). Temperature profile is shown in upper panel. The starting temperature for each experiment is 20 °C. The gas evolution rates of products during the early stage in the experiment using the 10-μm diameter orifice (Exp. I) are shown in C. Experimental conditions are listed in Table 1.

products from the gas-phase reactions are codeposited along with condensing RDX on the surface of the particles or sintered regions of the sample, and (3) some of these codeposited decomposition products initiate new reaction pathways in the condensed phase. The results also suggest that the rate of reaction of the condensed phase processes is more rapid in the sintered regions of RDX than on the surface of the original crystalline RDX particles.

SEM Microscopy. SEM pictures of a partially decomposed agglomerate of RDX particles (Figure 6) provide further insight into the processes involved in the decomposition of RDX below its melting point. Figure 6A shows a low magnification picture of the outer surface of a partially decomposed agglomerate of RDX particles. The particles separated slightly when removed from the reaction cell but maintained their relative positions and orientations. The surfaces of the particles located on the outer surface of the agglomerate have a rough appearance compared to the surface of the pristine RDX particles (Figure 6D). Closer inspection of region 2 (Figure 6B) and region 3 (Figure 6C) shows that the surface of the RDX particles that were on the outer surface of the agglomerate are roughened, whereas the surface of the RDX particles in the interior of the agglomerate remain smooth and similar to the surface of a pristine particle (Figure 6D). The surfaces of the particles that are located on the outer surface of the agglomerate, but are not directly exposed to the free volume of the reaction cell (6B), are also smooth. The sides of the largest particle in Figure 6B are smooth compared to its outer surface. The black and orange regions observed in optical micrographs are located in the roughened regions observed in the SEM pictures.

The location of the roughened surfaces in the RDX sample provides further insight into the reaction processes that control the decomposition of RDX below its melting point. The fact that the roughened surfaces are only observed on the outside of the sample agglomerate, which is exposed to the relatively large free volume of the reaction cell above the RDX sample, suggests that products formed in the gas-phase decomposition of RDX interact with the surface of the RDX particles and lead to the roughened surfaces. The location of the different morphological features also suggests that roughening is not simply due to sublimation and recondensation of RDX on the surface of the particles. For if this were the cause of the roughening, it would be expected to occur in a similar manner on the surface of particles located in both the interior and outer surface of the agglomerate, which it does not. Likewise, the location of the roughened surface also suggests that reactions that occur on the surface of the RDX particles are not due solely to RDX being located on the surface of the particle, but must involve the creation of some other compound, formed via reactions in the gas phase, that interacts with, and may deposit on, the surface of the RDX particles. In our STMBMS experiments this occurs preferentially on the outer surface of the agglomerate, because most of the volume in which the gas-phase reactions occur is in the free volume of the reaction cell

located above the surface of the agglomerate. In comparison, the free volume within the agglomerate is less, so the amount of RDX decomposition products available to react with the surface of the particles in the interior of the agglomerate will be less than those on its surface.

The roughened surfaces of the RDX particles located on an outer surface of the agglomerate, together with the accelerating rate of mass loss during the course of the decomposition experiments, indicates that the increasing rates of reaction are due to new reaction pathways developing on the surface of the RDX particles. From this perspective, the roughened surface would be created by decomposition occurring more rapidly at some locations than at others. Thus, the dimensions of the pockets in the roughened surface would suggest that the reaction regions may vary in size from 1 up to $\sim 20\mu$m at the point in time when the sampled was cooled and the reactions stopped.

Evolution Rates of Decomposition Products. Examining the identities and time-dependent rate of evolution of the products formed during an experiment provides further insight into the underlying processes that control the decomposition of RDX. The data collected in each of the STMBMS experiments listed in Table 1 has been quantified according to previously published procedures,[24,26] and the time-dependent rate of gas evolution from the reaction cell of each product has been calculated and is presented in Figures 7 and 8. The same type of relative ion formation probability and elemental mass balance constraints are used for quantification of the data presented in this paper as was used for previous analysis of RDX data.[10] The elemental mass balance for each experiment is within 4% of the nominal value. Table 2 lists the decomposition products measured during the STMBMS experiments (Exps. I−V).

Products associated with different reaction pathways are identified by separating their rates of gas evolution into temporally correlated groups. Some products may be associated with several different reaction pathways. The general temporal behavior of the GERs of products in Exps. I−IV may be characterized by a period of a relatively constant rate of evolution followed by a period of increasing rate of gas evolution. Closer examination of the temporal behavior of the GERs as the RDX nears depletion shows significant variation in the rates of evolution of the various products. During this period the GER of RDX decreases and the GERs of most of the other products increase. This increase in GER is more pronounced for some products (e.g., C_3H_9N) than others.

The relatively constant rate of formation of decomposition products during the earlier stage of each experiment persists for the longest period of time in Exp. I (Figures 7A and 8C). During this period most of the various products are formed at relatively low rates. The products not formed, or formed at very low rates, during this early period are those compounds with relatively high fractions of carbon and hydrogen: $(CH_3)_2NCHO$, $(CH_3)_2NNO$, and C_3H_9N. The constant rate of formation of H_2O, CO/N_2, CH_2O, NO, N_2O, NO_2, *s*-triazine, OST, and ONDNTA in Exp. I over a long period of time is proportional to the partial pressure of RDX vapor in the cell and indicates that these products are formed via reaction of RDX in the gas phase.

The GER of one of the products, *s*-triazine ($C_3H_3N_3$), is roughly proportional to the amount of RDX present in the gas phase during the entire course of each experiment (the GER of RDX is proportional to its partial pressure in the reaction cell). This indicates that *s*-triazine, formed during the early stage of the experiment, originates solely from the decomposition of RDX in the gas phase. The rate of evolution of OST during the early stage of each experiment is lower than that of *s*-triazine (the temporal behavior of the GERs of the products during the early stage of Exp. I is shown in Figure 8C). This behavior differs from the decomposition of RDX in the liquid phase in which OST is the major product formed in the direct decomposition of RDX.[10] Thus, elimination of 3HONO from RDX appears to be one of the main decomposition pathways of RDX in the gas phase. This is consistent with one of the low energy reaction pathways predicted by recent ab initio quantum chemistry calculations.[8] Decomposition of RDX in the liquid phase alters the direct decomposition of RDX and leads to the formation of OST. An example of this behavior is illustrated by comparing the *s*-triazine and OST GERs in Exp. I (Figure 7A). In the later stage of Exp. I, the OST GER grows and eventually becomes as large as the *s*-triazine GER. The GERs of the products formed by secondary reactions of HONO, H_2O, NO, and NO_2 are also constant during the early stage of the experiments (Figure 8C).

The other gas-phase reaction that occurs during the early stage of Exp. I leads to the formation of ONDNTA. The direct decomposition of RDX to form *s*-triazine provides the NO required for reaction with RDX to form ONDNTA via a substitution reaction, similar to its formation in experiments with RDX in the liquid phase (Pathway P3, Scheme 1).[11] Examination of the early stage of Exp. I (Figure 8C) shows that the GER of ONDNTA from the reaction cell lags the GERs of RDX and several of the more volatile decomposition products. This behavior is due to the ONDNTA that is formed in the very early stage of the experiment condensing on the RDX particles in the sample. As more ONDNTA accumulates on the surface of the RDX sample, its partial pressure within the reaction cell increases until it attains its quasi-equilibrium vapor pressure value. The dominant products formed in the decomposition of ONDNTA,[12] CH_2O and N_2O, are also formed at relatively constant rates during the early stage of the experiments, suggesting that ONDNTA decomposes in the gas phase in these experiments. However, previous studies on the decomposition of ONDNTA[12] show that it decomposes in the condensed phase at temperatures between 100 and 150 °C. Thus, the evolution of decomposition products from ONDNTA may occur from ONDNTA present in either the gas phase or on the surface of the RDX particles.

The GERs of the products associated with the two primary gas-phase reactions have similar behaviors under both higher confinement (Exp. II, Figure 7B) and higher temperature (Exps. III and IV, parts A and B of Figure 8) conditions. In each of these experiments the duration of the early stage is less than it is in Exp. I, but the general behavior of the products associated with each of these reaction pathways, *s*-triazine and ONDNTA, is similar.

At the end of the early stage, associated with gas-phase reactions, the gas evolution rates of all the products start to accelerate. This increasing rate of reaction coincides with the formation of the NVR on the surface of the RDX particles. The major products formed in the accelerating reaction process are: H_2O, N_2/CO, CH_2O, NO, and N_2O. The rates of evolution of the minor products such as NH_2CHO, $(CH_3)_2NCHO$, $(CH_3)_2NNO$, and C_3H_9N also increase continuously until the RDX is depleted. This behavior, taken together with the growth of the film of NVR on the surface of the particles in the hot-stage microscopy experiment, indicates that the rate of reaction during the later stages of each experiment is controlled by the reaction and growth of the NVR during the course of the experiment. Thus, the NVR may be considered a dynamic mixture of products formed by reaction with RDX. This dynamic NVR

mixture both reacts with RDX and itself decomposes to release gaseous products and form new reaction intermediates that remain in the NVR. The rapid increase in the GERs of most of the products as the amount of RDX present in the sample nears depletion is indicative of the competition between the reaction of the NVR with RDX and the decomposition of the NVR by itself.

The overall behavior of the GERs for the products from Exps. I−III is similar, whereas the GERs from Exp. IV (Figure 8B) in which the sample is closer to the melting point of RDX have additional features. One difference is the rapid evolution of a small amount of HCN when the sample first reaches its isothermal temperature. This may be due to differences in the chemical characteristics of the outer subsurface regions of the RDX particles compared to the inner portion of the particles. A similar effect on the initial decomposition rate of 2,4-dinitroimidazole (24DNI), due to water absorbed in the subsurface of the particles, has been observed.[27] The other difference is the delayed, but more rapid, increase in the rate of evolution of major decomposition products: H_2O, CO/N_2, CH_2O, NO, and N_2O. This delayed onset of gas evolution and the similarity of the products to those observed in the liquid-phase decomposition of RDX suggests that at 189 °C the RDX on the surface of the RDX particles in the vicinity of the NVR may liquefy. This would open the liquid-phase reaction pathways, previously reported[10] and listed in Scheme 1.

Interaction of the Dynamic NVR with RDX. To examine the interaction between RDX and the dynamic NVR in more detail, an experiment (Exp. V) was conducted in which RDX was mixed with NVR produced in a previous experiment and decomposed under conditions similar to those used for Exp. II. Comparison of the results from these two experiments shows that RDX decomposes more rapidly in the experiment with the mixture of RDX and NVR (Exp. V, Figure 7C) than in the experiment with RDX by itself (Exp. II, Figure 7B). The most obvious difference in the GERs of the products is the relatively high rate of evolution of products when the experiment with the RDX/NVR mixture first reaches the isothermal temperature of 179 °C. For example, the GER of N_2O in Exp. V is $\sim 1.5 \times 10^{-9}$ mol/s when the sample first reaches the isothermal temperature. This value is high compared to the similar period in Exp. II in which the GER for N_2O is $\sim 0.02 \times 10^{-9}$ mol/s. However, as Exp. II progresses the GER of N_2O just prior to depletion of RDX rises to a value of 2×10^{-9} mol/s, which is approximately the same as its initial rate of evolution in Exp. V. This is very strong evidence that reaction between RDX and the NVR becomes the dominant reaction process as the dynamic NVR accumulates in the sample during the course of an experiment.

The high GERs of the decomposition products in Exp. V when the sample first reaches its isothermal temperature indicates that the reaction process may involve the transport of RDX through the gas phase to the surface of the NVR where it reacts. The relatively modest growth in the GERs during Exp. V (e.g., the GER of N_2O rises from 1.5 to 3.5×10^{-9} mol/s) suggests that the rate of reaction may be limited by amount or exposed surface area of the dynamic NVR available during the course of an experiment.

Further insight into the nature of the reaction of RDX with the dynamic NVR and the decomposition of the NVR itself may be obtained by examining the GERs of RDX and the various products just prior to, and after, the depletion of RDX in each experiment. There are four distinguishing temporal features of the GERs during this period of each experiment. First, two of the products (NH_2CHO and C_3H_9N) have small, but significant, GERs after the RDX is depleted. This suggests that these products originate directly from decomposition of the dynamic NVR. Second, most of the products exhibit a rapid rise in their GER as the RDX nears depletion. Products with this characteristic include: NO, N_2O, NH_2CHO, $(CH_3)_2NCHO$, and $(CH_3)_2NNO$. Third, the GERs of RDX and $C_2H_2N_2O$ decrease as the RDX nears depletion. This suggests that the formation of $C_2H_2N_2O$ is related to vapor phase RDX and the presence of the dynamic NVR. The higher rate of formation of $C_2H_2N_2O$ in the experiment with the mixture of NVR and RDX (Figure 7C) is consistent with this idea. Thus, $C_2H_2N_2O$ may be formed via a reaction between RDX and the NVR on the surface of the NVR. Fourth, there is a shorter period during this final stage of the decomposition process in which the GER of one of the products (C_3H_9N) increases rapidly and the GER of another product (CH_2O) falls off as the other lower molecular weight products are still increasing (see CH_2O in Figure 7C). This suggests that during the final stage of the decomposition CH_2O may react with the dynamic NVR to form several of the other products (i.e., NH_2CHO and $(CH_3)_2NCHO$). These features of the temporal behaviors of the GERs during the final stage of the decomposition process provide some further qualitative understanding of the reactions that involve the NVR.

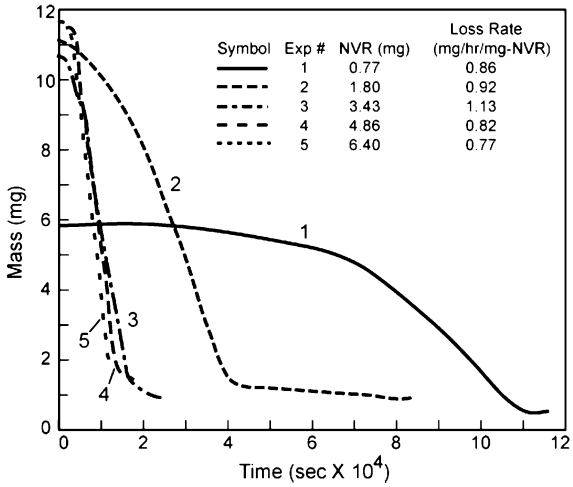

Figure 9. Sample mass vs time data from a series of five experiments in which RDX was added to the NVR remaining in the reaction cell from the previous experiment. The experiments were run at 180 °C using a reaction cell fitted with a 5-μm diameter orifice. The NVR formed in each experiment accumulated as a solid mass in the bottom of the reaction cell. The mass loss rates and amount of NVR present at the end of each experiment are listed in the table.

To examine the reactivity of the dynamic NVR a series of five experiments were run in which RDX was added to the NVR remaining in the reaction cell from the previous experiment. TGA data from the series of five experiments (Figure 9) shows that after accumulating NVR from two experiments the delay until onset of the rapid reactions associated with the dynamic NVR is essentially eliminated. After the first two experiments the bottom of the reaction cell was coated with dark-red islands of NVR. After the third experiment the bottom of the reaction cell was coated with a dark-red solid mass of NVR, whose effective exposed surface area did not increase further with the addition of residue from the fourth and fifth experiments. The NVR did not accumulate on the sides of the reaction cell above the location of the RDX sample, as had been observed for experiments using the larger 10- and 25-μm diameter orifices. The higher pressure of gases in experiments using smaller diameter orifices appears to confine the reactions involving RDX

SCHEME 2. Decomposition Pathways of RDX below Its Melting Point

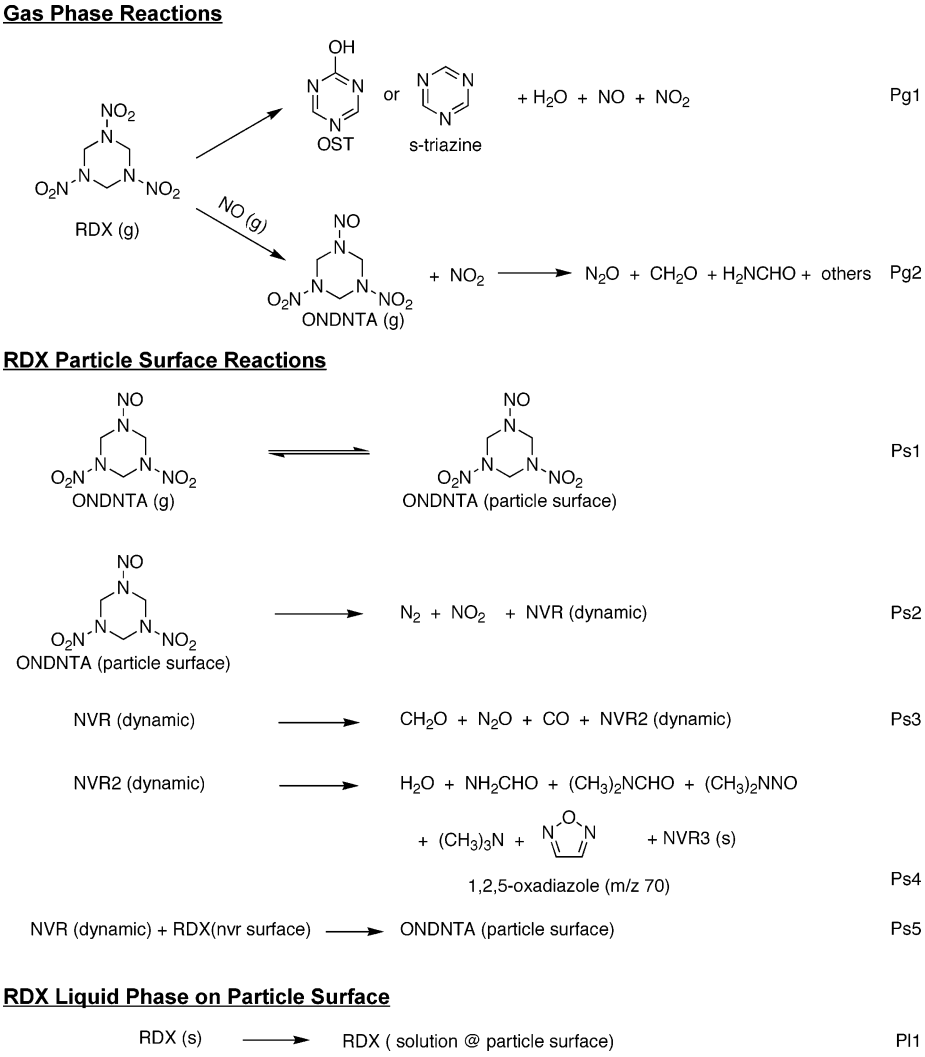

to regions near the sample. The accumulation of NVR during the first experiment had the biggest effect on changing the reaction rate, as would be expected, since the NVR must first nucleate via gas-phase reaction processes. In the final two experiments the surface area of the NVR located in the bottom of the reaction cell remained approximately the same. Thus, in the last two experiments the depth of the NVR sample grew by approximately 40% in each experiment.

Examining the data from the last three experiments shown in Figure 9 shows that the rate of mass loss due to RDX reacting with the NVR does not increase in proportion to the increase in the amount of NVR present in the bottom of the reaction cell. This indicates that reaction between the RDX and NVR involves reactions on the surface and/or subsurface of the NVR but not with the entire mass of NVR. Thus, one of the factors limiting the rate of reaction between RDX and the NVR may be the solubility of RDX in the NVR.

Discussion

The results from the STMBMS experiments with RDX below its melting point show that thermal decomposition reactions occur in three principal regions. These regions include: (1) RDX in the gas phase, (2) the surface of the RDX particles, and (3) in a liquid film formed on the surface of the RDX particles. Several different reaction pathways, as summarized by Scheme 2, control the decomposition process in each region.

Two reaction pathways account for the primary decomposition processes in the gas phase. One pathway is the direct reaction of RDX to form either OST or *s*-triazine and the corresponding decomposition products formed via the elimination of HONO and HNO from RDX: NO, NO_2, and H_2O. This reaction is similar to the direct reaction of RDX observed in the liquid-phase decomposition of RDX (Scheme 1). Elimination of 3 HONO to form *s*-triazine appears to be the more dominant reaction in the gas phase. One of these products, NO, is involved in the second reaction pathway in which NO replaces an NO_2 group to form the mononitroso analogue of RDX, ONDNTA. This reaction pathway is also similar to Pathway P3 in the liquid-phase decomposition (Scheme 1), in which ONDNTA decomposes to form CH_2O, N_2O, NH_2CHO, and several other gaseous products. The ONDNTA, having a vapor pressure similar to RDX, condenses on the surface of the RDX particles. During the initial stage of the experiment, the rate of evolution of ONDNTA from the reaction cell is quite low until a quasi-equilibrium is established between ONDNTA in the condensed and gas phases (Pathway Ps1, Scheme 2).

The deposition of ONDNTA from gas-phase reactions onto the surface of the RDX particles opens new reaction pathways (Pathways Ps2−Ps5). Previous studies on the decomposition of ONDNTA[12] have shown that it decomposes in a series of steps. First, N_2 and NO_2 are eliminated rapidly from ONDNTA to form an intermediate, NVR(dynamic). Next, CH_2O, N_2O, and

CO are gradually eliminated from the NVR(dynamic) intermediate to form a second intermediate, NVR2(dynamic) (Pathway Ps3). This second intermediate eventually is transformed to a state in which a new set of reactions occur, leading to the formation of H_2O, $(CH_3)_2NCHO$, $(CH_3)_2NNO$, and $(CH_3)_3N$ and another nonvolatile residue, NVR3, that remains at the completion of an experiment (Pathway Ps4). The same set of products is observed during the decomposition of RDX below its melting point in the STMBMS experiments as was observed in the STMBMS experiments with ONDNTA. In each of the STMBMS experiments with RDX, this set of products is observed during the later stage of each experiment when the rates of reaction are increasing in an "autocatalytic-like" manner. During the later stages of the STMBMS experiments reactions are observed to occur on the surface of the RDX particles. This is consistent with the growth of an orange-colored film on the surface of the RDX particles (Figures 4 and 5) and the roughened appearance of the surface of the RDX particles located on the outer surface of the agglomerated sample (SEM pictures, Figure 6). Thus, the reaction process during the later stages of each experiment is dominated by the reactions of ONDNTA and its decomposition intermediates on the surface of the RDX particles.

The reaction intermediates formed in the decomposition of ONDNTA, NVR(dynamic) and NVR2(dynamic), are referred to as dynamic because these intermediates are not true compounds but are actually mixtures of remnants from decomposed RDX and ONDNTA molecules that most likely link to form a nonvolatile residue. The nature of these NVR intermediates changes during the course of the decomposition process and thus may be referred to as dynamic.

The NVR(dynamic) intermediate located on the surface of the RDX particles can react with RDX at the interface to form more ONDNTA and lead to an accelerating rate of reaction (Pathway Ps5), as observed during the STMBMS experiments. As the decomposition process progresses this reaction pathway leads to the accumulation of NVR(dynamic) on the surface of the RDX particles. The accumulation of NVR(dynamic) on the surface of the RDX particles and the accelerating rate of reaction observed during the course of an experiment leads to the question of how NVR(dynamic) interacts with the RDX.

To answer this question, an experiment in which RDX was transported through the gas phase to the surface of the NVR was conducted. In a sequence of RDX decomposition steps, NVR was accumulated on the bottom of the STMBMS reaction cell. Once the exposed surface area of the NVR achieved a constant value the rate of reaction also attained a constant value (Figure 9). Thus, the rate of reaction of RDX with the NVR is limited by the surface area of the NVR. The increasing depth of the NVR does not result in an increased rate of reaction with RDX, indicating that the reaction between the NVR and the RDX occurs either on the surface of the NVR or in a near subsurface region of the NVR. These results confirm that the accelerating rate of reaction is due to the accumulation of NVR(dynamic) on the surface of the RDX particles. However, the results also suggest that the dissolution of RDX into the NVR film may be limited to a thin layer of the NVR(dynamic) near the NVR/RDX interfacial boundary.

The formation of the NVR(dynamic) film on the surface of the RDX particles leads to the formation of new region on the surface of the RDX particles, located between the NVR(dynamic) film and a boundary of the RDX particle that still retains its crystalline properties. This region can be considered a thin film of RDX mixed with decomposition products to form a liquid solution. A new set of reaction pathways may occur in this thin film region as indicated by Pathway Pl1 in Scheme 2. The reaction pathways available for decomposition of RDX in this region are those associated with the decomposition of RDX in the liquid phase (Scheme 1). The accelerating rate of reaction that is expected from the liquefaction of the RDX is most pronounced in the experiment in which the temperature of the sample approaches the melting point of RDX (Exp. IV).

The reaction processes outlined in Scheme 2 can be affected by the pressure of gases surrounding the RDX particles. This difference may be observed by comparing the location of the growth of the NVR in the STMBMS experiments (Figure 5) with its growth in the hot-stage experiment (Figure 4). In the STMBMS experiment the lower gas pressure allows greater movement of both RDX and its decomposition products in the sample. This leads to the redeposition of RDX and its decomposition products in regions between original RDX particles. Decomposition via the RDX particle surface reactions (Pathways Ps1−Ps5) occurs initially in these regions. In contrast, the higher gas pressure (0.237 MPa of gaseous decomposition products in the microreactor) used in the hot-stage experiments limits gas-phase transport of RDX and its decomposition products, resulting in a more uniform formation of the NVR(dynamic) film on the surface of the RDX particles.

In the series of experiments conducted by Batten[17−21] the rate and kinetics of the decomposition of RDX below the melting point were influenced by the RDX sample geometry. The effect was attributed to interactions between gaseous decomposition products and the remaining solid RDX sample. At later stages in the decomposition, localized liquefaction of the remaining RDX is also noted for samples originally packed within small sample tubes, while for samples initially spread over the bottom of the large reaction flask, uniform liquefaction is observed throughout the sample. In both cases, the samples are maintained below the melting point of RDX and the liquefaction is attributed to formation of an intermediate that combines with RDX to form a solution with a lower melting point than RDX. Results from these experiments also indicated formation of a colored NVR that acted as a positive catalyst for the decomposition. Experiments using NO as a backfilling gas also showed a positive catalyst effect. These results are consistent with the decomposition pathways determined in the present experiments and summarized in Scheme 2. The increased rate of reaction due to the addition of NO can be attributed to increased rate of reaction Pg2 and a more rapid accumulation of ONDNTA on the RDX sample. Their observation of the appearance of a colored residue is consistent with reactions that occur on the surface of the RDX particles via pathways Ps2−Ps5. The observed liquefaction late in the experiments can be attributed to the pathway Pl1 in Scheme 2 that opens the reaction pathways associated with decomposition of RDX in the liquid phase (Scheme 1). Once the RDX becomes molten, NO may dissolve in the molten mixture and increase the rate of decomposition of the sample via reaction pathway P3 in Scheme 1.

Conclusions

The decomposition of RDX below its melting point has been examined. Gas-phase reactions are predominant in the early stages of an experiment. Reactions in the gas phase are similar to those previously observed for RDX in the liquid phase above its melting point. These reactions include the formation of OST, *s*-triazine, H_2O, NO, and NO_2 via the elimination of HONO and HNO from an RDX molecule and the formation of ONDNTA and NO_2 via an NO replacement reaction with RDX.

ONDNTA decomposes to form predominantly CH_2O and N_2O. NH_2CHO may also be formed in the gas-phase decomposition of ONDNTA.

In our STMBMS experiments, products from the gas-phase reactions, such as ONDNTA and formamide, condense along with RDX on the surface of the RDX particles and in regions between the RDX particles. This mixture of compounds on the surface of the RDX particles opens new reaction pathways that occur on the surface of the particles. The deposited material initially nucleates and grows in reactive islands on the surface of the particles. Reactions are more likely to occur on the surface of particles located in areas of the sample surface that are exposed to larger volumes containing RDX vapor, which can decompose.

The reactions on the surface of the particles lead to the formation of a colored nonvolatile residue on the surface of the RDX particles. At lower pressures, diffusion in the gas phase is greater and leads to the deposition of RDX and the decomposition products in regions separate from the original particles, where the NVR is observed to grow first. At higher pressures (0.1−0.2 MPa), diffusion of RDX and the decomposition products is limited due to the surrounding gas and they are confined in a region close to the RDX surface, which results in the growth of a more uniform film of NVR on the surface of the RDX particles.

The NVR reacts directly with RDX and leads to a range of different decomposition products, of which CH_2O and N_2O are the most prevalent. RDX decomposes most rapidly when it is contact with the NVR. Reaction between RDX and the NVR can occur via either transport of RDX through the gas phase to the surface of the NVR or at the boundary between the NVR and the RDX on the surface of the RDX particles. It is possible that the RDX may react not only at the surface of the NVR but may also dissolve and react within a layer below the NVR surface.

The NVR is a dynamic mixture in which its constituents change during the course of the decomposition process. During the course of an experiment, RDX reacts with the NVR to form ONDNTA, which in turn decomposes to form gaseous products and add more material to the NVR. There is competition between reaction processes involving RDX and the NVR and the decomposition of the NVR by itself. This competition manifests itself in the increased rate of release of compounds with high levels of hydrogen, such as $(CH_3)_2NNO$, $(CH_3)_2$-NCHO, and $(CH_3)_3N$, when the RDX nears depletion at the end of an experiment. This suggests that the structures in the NVR that lead to the formation of these compounds may be involved in the reaction between RDX and the NVR.

As the temperature of the RDX powder nears the melting point of RDX, regions of the sample become molten, probably in the vicinity of the NVR, and the reaction process more closely resembles that observed during the decomposition of RDX in the liquid phase. Thus, at temperatures well below its melting point, the decomposition of RDX is controlled initially by sublimation of RDX and its decomposition in the gas phase and later by reactions with the NVR in localized regions on the surface of the RDX particles.

Acknowledgment. The authors thank L. Johnston for assistance with running experiments and collecting the data, D. Wiese-Smith and G. A. Goelzer for assistance in quantifying the experimental data. J. Woods, S. Mack, and K. Anderson for assistance in developing the modified reaction cell and flow rate calibration procedures. M. Kennedy for collecting the hot-stage microscopy data, N. Yang and J. Chames for the SEM micrographs, and Huffman Laboratories of Golden, CO, for the quantitative C/H/N microanalysis of the RDX NVR. This research was supported by the U.S. Army Research Office Project 43381-CH and a joint Memorandum of Understanding between the Department of Defense Office of Munitions and the U.S. Department of Energy.

References and Notes

(1) Robertson, A. J. B. *Trans. Faraday Soc.* **1949**, *45*, 85.
(2) Cosgrove, J. D.; Owen, A. J. *Chem. Commun.* **1968**, 286.
(3) Schroeder, M. A. Critical Analysis of Nitramine Decomposition Results: Some Comments on Chemical Mechanisms. In *16th JANNAF Comb. Mtg.*; Chemical Propulsion Information Agency, 1979; Vol. 308, II., p 17.
(4) Schroeder, M. A. Critical Analysis of Nitramine Decomposition Data: Activation Energies and Frequency Factors for HMX and RDX Decomposition. In *17th JANNAF Comb. Mtg.*; Chemical Propulsion Information Agency, 1980; Vol. 329 , II., p 493.
(5) Schroeder, M. A. Critical Analysis of Nitramine Decomposition Data Product Distributions From HMX and RDX Decomposition. In *18th JANNAF Mtg.*; Chemical Propulsion Information Agency, 1981; Vol. 347, II., p 395.
(6) Adams, G. F.; Shaw, R. W. *Annu. Rev. Phys. Chem.* **1992**, *43*, 311.
(7) Melius, C. F. *J. Phys.* **1987**, *c4*, 341.
(8) Chakraborty, D.; Muller, R. P.; Dasgupta, S.; Goddard, W. A. *J. Phys. Chem. A* **2000**, *104*, 2261.
(9) Zhao, X.; Hintsa, E. J.; Lee, Y. T. *J. Chem. Phys.* **1987**, *88*, 801.
(10) Behrens, R.; Bulusu, S. *J. Phys. Chem.* **1992**, *96*, 8877.
(11) Behrens, R.; Bulusu, S. *J. Phys. Chem.* **1992**, *96*, 8891.
(12) Behrens, R.; Bulusu, S. The Importance of Mononitroso Analogues of Cyclic Nitramines to the Assessment and the Safety of HMX-Based Propellants and Explosives. In *Challenges in Propellants and Combustion 100 Years after Nobel*; Kuo, K. K., Ed.; Begell House, Inc.: New York, 1997; p 275.
(13) Brill, T. B.; Brush, P. J.; Kinloch, S. A.; Gray, P. *Philos. Trans. R. Soc. London, Ser. A* **1992**, *15*, 377.
(14) Long, G. T.; Vyazovkin, S.; Brems, B. A.; Wight, C. A. *J. Phys. Chem. B* **2000**, *23*, 2570.
(15) Cosgrove, J. D.; Owen, A. J. *Combust. Flame* **1974**, *22*, 13.
(16) Cosgrove, J. D.; Owen, A. J. *Combust. Flame* **1974**, *22*, 19.
(17) Batten, J. J. *Austr. J. Chem.* **1972**, *25*, 2337.
(18) Batten, J. J.; Murdie, D. C. *Austr. J. Chem.* **1970**, *23*, 737.
(19) Batten, J. J.; Murdie, D. C. *Austr. J. Chem.* **1970**, *23*, 749.
(20) Batten, J. J. *Austr. J. Chem.* **1971**, *24*, 945.
(21) Batten, J. J. *Austr. J. Chem.* **1971**, *24*, 2025.
(22) Bradley, J. N.; Butler, A. K.; Capey, W. D.; Gilbert, J. R. *J. Chem. Soc., Faraday Trans. I* **1977**, *73*, 1789.
(23) Behrens, R. Thermal Decomposition Processes of Energetic Materials in the Condensed Phase at Low and Moderate Temperatures. In *Overviews of Recent Research on Energetic Materials*; Shaw, R. W., Brill, T. B., Thompson, D. L., Eds.; World Publications Inc., 2005.
(24) Behrens, R., Jr. *Rev. Sci. Instr.* **1987**, *58*, 451.
(25) Behrens, R., Jr. *Int. J. Chem. Kinet.* **1990**, *22*, 135.
(26) Behrens, R., Jr. *Int. J. Chem. Kinet.* **1990**, *22*, 159.
(27) Behrens, R.; Minier, L.; Bulusu, S. Coupling Experimental Data and a Prototype Model to Probe the Physical and Chemical Processes of 2,4-Dintiroimidazole Solid-Phase Thermal Decomposition. In *34th JANNAF Combustion Subcommittee Meeting*; CPIA, Ed.; CPIA Publication # 662: West Palm Beach, FL, 1997; Vol. 1, p 549.
(28) Anderson, K.; Homsy, J.; Behrens, R.; Bulusu, S. *11th International Detonation Symposium* **1998**, *1*, 239.
(29) Behrens, J., R.; Bulusu, S. *29th JANNAF Combustion Meeting* **1992**, *CPIA Publ. 573, Vol. II*, 453.